A&A 452, L15–L18 (2006)
DOI: 10.1051/0004-6361:20065182

Astronomy & Astrophysics

LETTER TO THE EDITOR

A comparison of solar proxy-magnetometry diagnostics

J. Leenaarts[1], R. J. Rutten[1,2], M. Carlsson[2,3], and H. Uitenbroek[4]

[1] Sterrekundig Instituut, Postbus 80 000, 3508 TA Utrecht, The Netherlands
e-mail: J.Leenaarts@astro.uu.nl
[2] Institute of Theoretical Astrophysics, University of Oslo, PO Box 1029, Blindern, 0315 Oslo, Norway
[3] Center of Mathematics for Applications, University of Oslo, PO Box 1053, Blindern, 0316 Oslo, Norway
[4] NSO/Sacramento Peak, PO Box 62, Sunspot, NM 88349–0062, USA

Received 10 March 2006 / Accepted 26 April 2006

ABSTRACT

Aims. We test various proxy-magnetometry diagnostics, i.e., brightness signatures of small-scale magnetic elements, for studying magnetic field structures in the solar photosphere.
Methods. Images are numerically synthesized from a 3D solar magneto-convection simulation for, respectively, the G band at 430.5 nm, the CN band at 388.3 nm, and the blue wings of the Hα, Hβ, Ca II H, and Ca II 854.2 nm lines.
Results. Both visual comparison and scatter diagrams of the computed intensity versus the magnetic field strength show that, in particular for somewhat spatially extended magnetic elements, the blue Hα wing presents the best proxy-magnetometry diagnostic, followed by the blue wing of Hβ. The latter yields higher diffraction-limit resolution.
Conclusions. We recommend using the blue Hα wing to locate and track small-scale photospheric magnetic elements through their brightness appearance.

Key words. Sun: magnetic fields – Sun: granulation – Sun: photosphere

1. Introduction

Small bright features that appear within intergranular lanes on solar photospheric filtergrams taken in the G band of CH lines at 430.5 nm are habitually used as proxy diagnostics to study small-scale magnetic structure (e.g., Muller & Roudier 1984; Berger & Title 2001; Berger et al. 2004). Such "G-band bright points" have been faithfully reproduced through spectral synthesis applied to 3D magneto-convection simulations of the solar photosphere, at disk center by Schüssler et al. (2003) and Shelyag et al. (2004), and also towards the solar limb by Carlsson et al. (2004). Photospheric magnetic elements appear as bright points also in the wings of strong lines including Ca II H & K, the Ca II infrared triplet, the Mg I b triplet, and the hydrogen Balmer lines. The CN band at 388.3 nm shows them also (Rutten et al. 2001), according to Zakharov et al. (2005) even at appreciably higher contrast than the G band but Uitenbroek & Tritschler (2006) attribute this difference instead to the erroneous inclusion of the Hζ line in the filter passband of Zakharov et al. (2005).

In Leenaarts et al. (2006, henceforth Paper I) we compared bright-point visibility in the G band and the blue wing of Hα using Dutch Open Telescope images. We found that bright points may appear prominently in the Hα wing even when their G-band counterparts are only intermittently present or fully absent. Synthetic Hα images computed from a magneto-convection simulation showed good qualitative agreement with these observations, although not fully matching the observed Hα bright-point contrast. Further analysis demonstrated how magnetic-element brightness enhancement, low granulation contrast, and absence of granular brightness reversal combine to make magnetic elements stand out clearly in this diagnostic.

The Hβ line has similar formation characteristics as Hα while its shorter wavelength (486.1 nm versus 656.3 nm for Hα) yields better angular resolution at the telescopic diffraction limit. This motivates the test of Hβ as proxy-magnetometer reported here, performed through image synthesis from a numerical simulation. We extend this appraisal of bright-point response to the wings of Ca II H and Ca II 854.2 nm, selecting the wavelengths shown in Fig. 1. The extended Ca II H & K wings merit testing since they provide well-spaced sampling throughout the photosphere (Sheminova et al. 2005). Ca II 854.2 shows Hα-like mottles at line center and bright points in its wings, for example in IBIS narrow-band imagery[1], making direct comparison with Hα of interest. We add Hα, G-band and CN-band image synthesis for comparison.

2. Methods

We use the same snapshot from a three-dimensional magneto-hydrodynamical convection simulation by Stein & Nordlund (1998) used by also by Carlsson et al. (2004), Uitenbroek & Tritschler (2006), and in Paper I. The simulation included LTE ionization and non-grey LTE radiative transfer. It was started with a homogeneous vertical magnetic field of 250 G. The snapshot used here resulted after considerable evolution in which the field was swept into intergranular concentrations. The simulation snapshot has an horizontal extent of 6×6 Mm and ranges in height from 2.5 Mm below to 0.5 Mm above mean optical depth $\langle \tau_{500} \rangle = 1$. Figure 2 shows the magnitude of the magnetic field at the local $\tau_{500} = 1$ surface. The field has ribbon-shaped kilo-Gauss concentrations along edges of mesogranules and strengths of order 30 G within granular interiors. The right-hand panel results from applying a binary mask passing all pixels with $|B| > 1$ kG (white). We call these locations magnetic elements, and refer to the mask complement (black) as granulation.

[1] http://www.arcetri.astro.it/science/solare/IBIS/ibis.gallery.html

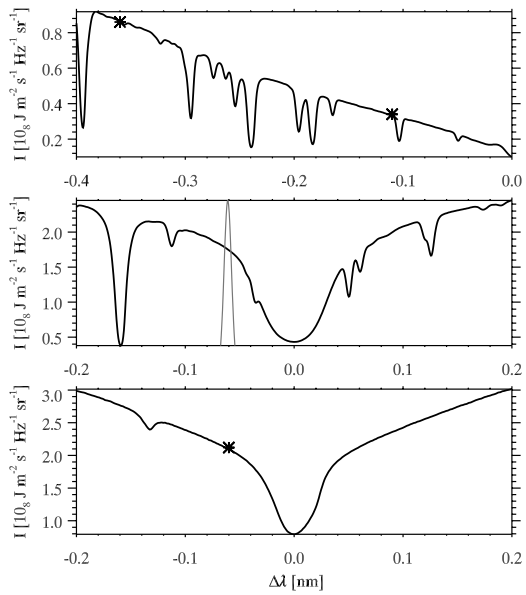

Fig. 1. Spatially averaged disk-center intensity profiles from the NSO Fourier Transform Spectrometer atlas calibrated by Neckel & Labs (1984). *Upper panel*: blue wing of Ca II H. The two asterisks mark the wavelengths used for image synthesis. *Middle panel*: Hβ, with the transmission function used for image synthesis. *Lower panel*: Ca II 854.2. The asterisk marks the synthesis wavelength.

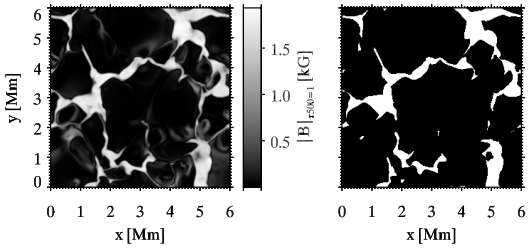

Fig. 2. *Left*: map of the absolute field strength at $\tau_{500} = 1$. *Right*: mask showing all locations in the 3D simulation with absolute magnetic field strength at $\tau_{500} = 1$ exceeding 1 kG.

We perform 3D LTE radiative transfer calculations on this simulation cube using the RH code of Uitenbroek (2001) to synthesize disk-center intensity images in the inner and outer blue wing of Ca II H (at $\Delta\lambda = -0.11$ nm and -0.36 nm), the blue wing of Ca II 854.2 ($\Delta\lambda = -0.09$ nm) and the blue wing of Hβ ($\Delta\lambda = -0.06$ nm). The Ca II H and Ca II 854.2 images were computed for a single wavelength, the Hβ image was synthesized by spectral integration over a Gaussian passband of 0.009 nm *FWHM*. Figure 1 shows these spectral selections. They are free of blends.

The validity of LTE was confirmed for the Hβ wing through detailed 2D NLTE computation as in Paper I. The validity of LTE for the Ca II lines has not been tested, but in the FAL-C model of Fontenla et al. (1993) both lines form very close to LTE at the wing wavelengths used here, suggesting that LTE is also a good approximation for our simulation cube.

We also employ synthetic CN-band and G-band images computed by Uitenbroek & Tritschler (2006) from the same simulation cube through spectrally integrating the emergent intensity over 1 nm *FWHM* generalized Lorentzian passbands centered at the respective bandheads, and a synthetic Hα-wing image from Paper I for a 0.025 nm *FWHM* Gaussian passband centered at $\Delta\lambda = -0.08$ nm from line center. These different diagnostics all form approximately 100 km higher than the local continuum (Uitenbroek & Tritschler 2006; Leenaarts et al. 2006), except for the inner Ca II H wing which originates about 250 km above $\langle\tau_{500}\rangle = 1$ (Leenaarts & Wedemeyer-Böhm 2005).

3. Results

Figure 3 shows the computed synthetic intensity images ordered in wavelength from top to bottom. The columns contain different image displays: without spatial degradation (left), convoluted with an Airy function corresponding to a 1 m telescope aperture (center), and difference images (right). The latter are obtained as $I_{\rm diff} = I/\langle I\rangle - C\, I_{\rm cont}/\langle I_{\rm cont}\rangle$ by subtracting images synthesized with 1-m smearing at a nearby continuum wavelength from the smeared image in the center column applying empirically determined factors C following e.g., Berger et al. (1998). The continua used in these subtractions are at 388.3 nm for the CN band ($C = 0.7$) and the outer Ca II H wing ($C = 0.5$), 430.5 nm for the G band ($C = 0.65$), 500 nm for Hβ ($C = 0.35$), and 654 nm for Hα ($C = 0.2$) and Ca II 854.2 ($C = 0.4$). Figure 3 has no difference panel for the inner Ca II H wing because it shows reversed instead of normal granulation so that subtraction does not help. The upper number in the upper-left corner of each panel is the relative rms intensity variation $\sqrt{\sum_n (I - \langle I\rangle)^2/\langle I\rangle^2/n}$ of the granulation alone. The lower number specifies the average contrast of the bright points over the granulation defined as $\langle I_{\rm BP}\rangle/\langle I_{\rm GR}\rangle - 1$.

Visual inspection of the images and comparison with Fig. 2 shows that the Hα wing is the best diagnostic to identify magnetic elements, in particular less compact ones. Its low granular intensity modulation makes the bright points stand out even though their contrast over the granulation is rather small. The next best is the Hβ wing. In the G band and the CN band the more extended field concentrations are not brighter than the granulation, for example at $(x, y) = (5, 0.5)$ and $(4.5, 5.5)$ (cf. Fig. 8 and the discussion thereof in Berger et al. 2004). The outer Ca II H wing shows a scene somewhat between the molecular bands and Hβ, with compact magnetic elements appearing bright and the more extended elements only slightly brighter than granules. The bright points in the inner Ca II H wing are more diffuse and have different morphology than in the other diagnostics.

All diagnostics perform better in the difference images in the third column of Fig. 3, but also in these the G band, CN band and outer Ca II H wing perform worse than the Balmer wings. In Hβ the magnetic areas appear almost the same as in Hα but sharper, whereas the Ca II 854.2 wing suffers from lower resolution than Hα. Note that all difference images show a Y-shaped brightness structure centered at $(x, y) = (1, 2)$ which results at least partially not from magnetism but from the combination of a dark granular lane in the continua and reversed-granulation brightening at larger height.

Figure 4 shows scatter diagrams of normalized intensity against magnetic field strength per smeared-image pixel. The first column shows these for the images in the center column of Fig. 3. All diagnostics show a large cluster of pixels at near-zero field strength, caused by the granulation. There is a second cluster at high field strengths, caused by the magnetic elements. The higher the intensity of the second cluster is raised above the granulation, the better is the corresponding diagnostic as a proxy magnetometer. This means in terms of intensity distribution functions (DF) that the more the low B DF (blue) is separated from the high B DF (red), the better is the corresponding

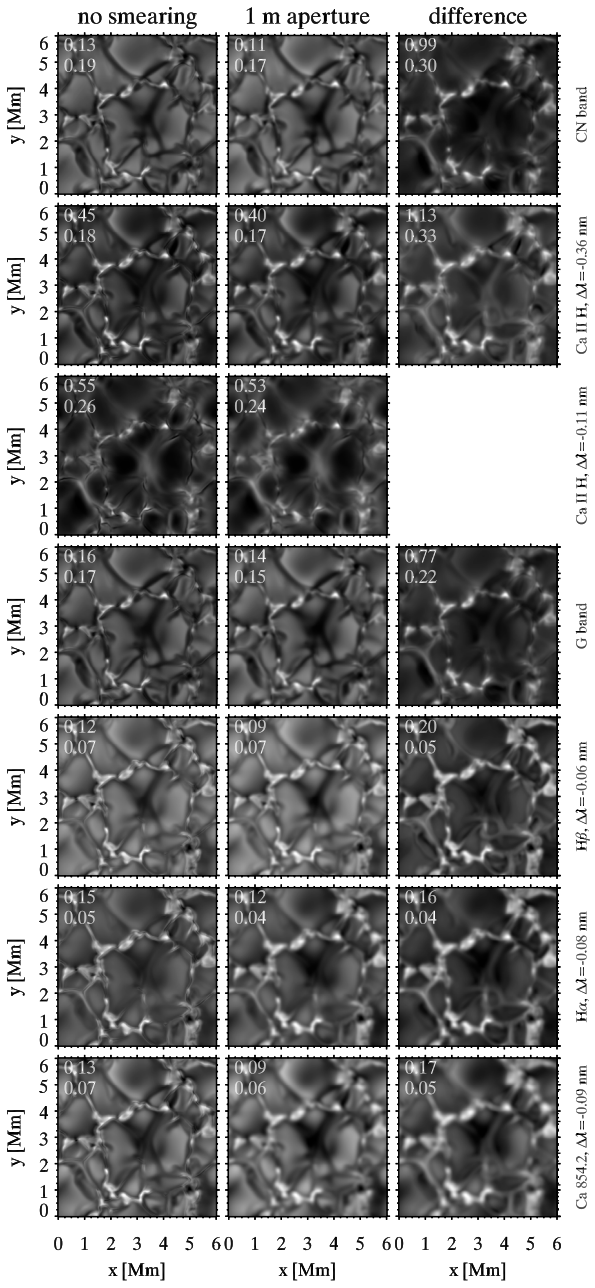

Fig. 3. Synthetic images for different spectral diagnostics identified per row at the right. The CN-band and G-band images are taken from Uitenbroek & Tritschler (2006). All images are grey-scaled to maximum display contrast. The rms intensity variation of the granulation (upper number) and the mean intensity excess of the bright points over the granulation (lower number) is indicated in each upper-left corner. *Left*: no spatial smearing. *Middle*: smeared with an Airy function corresponding to 1-m aperture. *Right*: image constructed by subtracting a scaled synthetic continuum image from the one in the center column.

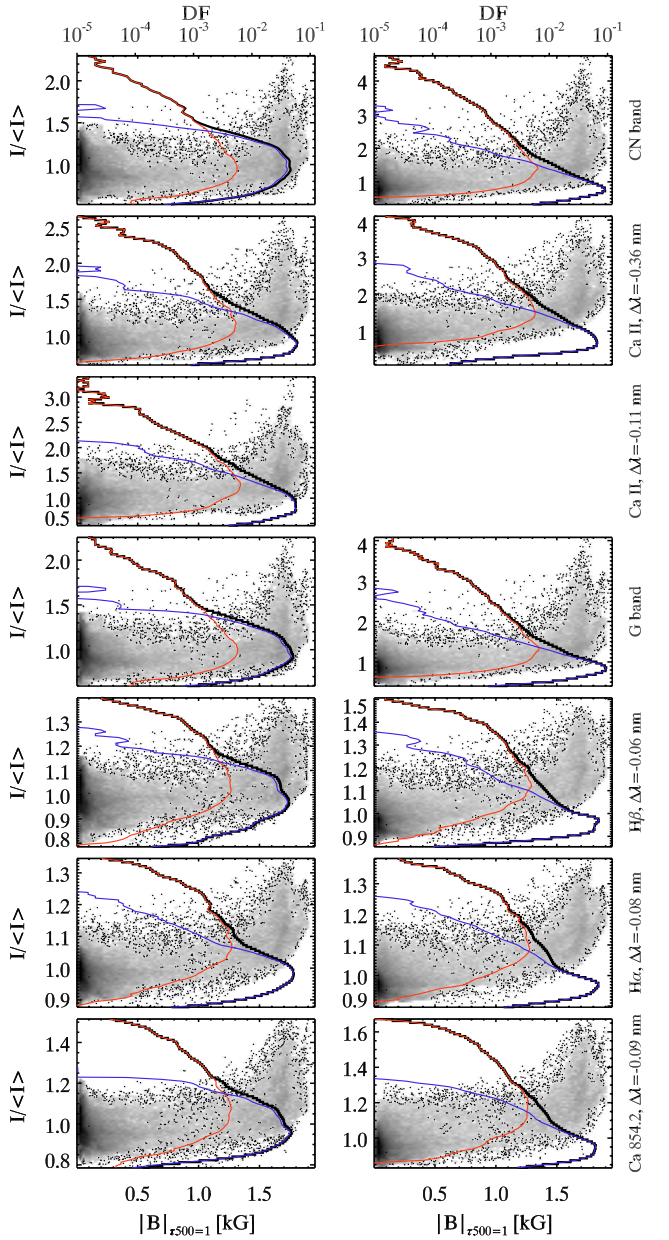

Fig. 4. Scatter diagrams of normalized intensity $I/\langle I\rangle$ versus magnetic field strength at $\tau_{500} = 1$ per pixel. To avoid plot overcrowding an inverted logarithmic grayscale is used, i.e., black areas have the highest point density. *Left*: intensity for 1 m aperture. *Right*: difference image. The curves indicate the normalized intensity distribution function for the corresponding image on a logarithmic scale shown at the top. *Black*: all pixels. *Blue*: pixels with $|B|_{\tau500=1} < 1$ kG. *Red*: with $|B|_{\tau500=1} > 1$ kG.

diagnostic as a proxy-magnetometer. Hα performs best in this regard. The diagrams in the second column show that subtracting continuum images greatly improves the bright-point visibility, raising the strong-field-pixel cluster above the granulation also for the outer Ca II H, Hβ, and Ca II 854.2 wings.

4. Discussion and conclusion

We conclude that the blue wing of Hα provides the best magnetic-element visibility. Second best is the blue wing of Hβ which offers, especially in the difference image, similar bright-point visibility at higher resolution. The other diagnostics suffer from lower resolution (Ca II 854.2), contamination with reversed granulation (inner Ca II H wing), or lack of enhancement in extended field concentrations (G band, CN band, outer Ca II H wing).

The reasons why the blue Hα wing performs so well were analyzed in detail in Paper I. They are a combination of low Planck function sensitivity to temperature, steep-wing Doppler compensation of granular temperature contrast, a deep opacity gap in the upper photosphere due to high excitation energy, small brightness response to temperature increase through

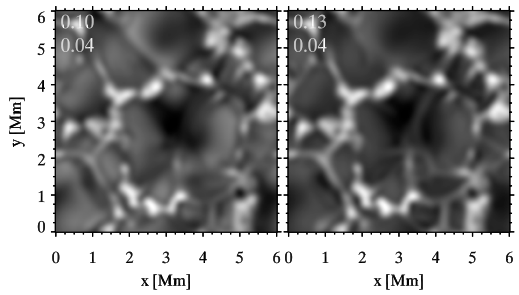

Fig. 5. Intensity and difference images for the Hα wing, convoluted with an Airy function corresponding to the Solar-B aperture of 50 cm. *Left*: Hα wing intensity. *Right*: Hα wing minus continuum. The rms intensity variation of the granulation (upper number) and the mean intensity excess of the bright points over the granulation (lower number) is indicated in each upper-left corner.

concomitant opacity increase, and reduction of collisional broadening within magnetic elements. These factors combine to brighten magnetic elements against a very "flat" non-reversed granular background in Hα. The same effects (except the first) apply also to Hβ.

In hindsight, the absence of reversed granulation in Hβ was already described by Evans & Catalano (1972) as absence of "oddities" affecting the Ca II H & K and Mg I b wings. They regarded Hβ as non-peculiar, but in fact reversed granulation results naturally from convection into a radiative overshoot layer (Leenaarts & Wedemeyer-Böhm 2005); its absence in the Balmer lines is peculiar. At the time, Thomas (1972) offered a complex NLTE interpretation in an accompanying note, but the actual explanation (given in Paper I) is simple and does not involve NLTE.

The Balmer line wings have the drawback of requiring narrower spectral passband than the molecular bands. They are also more susceptible to showing overlying chromospheric mottles than the molecular bands and the wings of H & K. Nevertheless, the blue Hα wing turns out the best proxy-magnetometer to locate and track spatially extended magnetic elements. We so champion this "chromospheric" line as photospheric diagnostic. Figure 5 shows synthetic Hα images at the resolution of the 50-cm Solar-B telescope. It will be of interest to compare Solar-B tunable-filter imaging in the wing of Hα with Solar-B scanning magnetometry. The first may complement the second as high-cadence full-field diagnostic.

References

Berger, T. E., & Title, A. M. 2001, ApJ, 553, 449
Berger, T. E., Löfdahl, M. G., Shine, R. A., & Title, A. M. 1998, ApJ, 506, 439
Berger, T. E., Rouppe van der Voort, L. H. M., Löfdahl, M. G., et al. 2004, A&A, 428, 613
Carlsson, M., Stein, R. F., Nordlund, Å., & Scharmer, G. B. 2004, ApJ, 610, L137
Evans, J. W., & Catalano, C. P. 1972, Sol. Phys., 27, 299
Fontenla, J. M., Avrett, E. H., & Loeser, R. 1993, ApJ, 406, 319
Leenaarts, J., & Wedemeyer-Böhm, S. 2005, A&A, 431, 687
Leenaarts, J., Rutten, R. J., Sütterlin, P., Carlsson, M., & Uitenbroek, H. 2006, A&A, 449, 1209 (Paper I)
Muller, R., & Roudier, T. 1984, Sol. Phys., 94, 33
Neckel, H., & Labs, D. 1984, Sol. Phys., 90, 205
Rutten, R. J., Kiselman, D., Rouppe van der Voort, L., & Plez, B. 2001, in Advanced Solar Polarimetry – Theory, Observation, and Instrumentation, ASP Conf. Ser., 236, 445
Schüssler, M., Shelyag, S., Berdyugina, S., Vögler, A., & Solanki, S. K. 2003, ApJ, 597, L173
Shelyag, S., Schüssler, M., Solanki, S. K., Berdyugina, S. V., & Vögler, A. 2004, A&A, 427, 335
Sheminova, V. A., Rutten, R. J., & Rouppe van der Voort, L. H. M. 2005, A&A, 437, 1069
Stein, R. F., & Nordlund, A. 1998, ApJ, 499, 914
Thomas, R. N. 1972, Sol. Phys., 27, 303
Uitenbroek, H. 2001, ApJ, 557, 389
Uitenbroek, H., & Tritschler, A. 2006, ApJ, 639, 525
Zakharov, V., Gandorfer, A., Solanki, S. K., & Löfdahl, M. 2005, A&A, 437, L43